SUPPLEMENTARY INFORMATION

Controlling the Photon Number Coherence of Solid-state Quantum Light Sources for Quantum Cryptography

Yusuf Karli[1*†], Daniel A. Vajner[2†], Florian Kappe[1†], Paul C. A. Hagen[3], Lena M. Hansen[4,5], René Schwarz[1], Thomas K. Bracht[6,7], Christian Schimpf[8], Saimon F. Covre da Silva[8], Philip Walther[4,5], Armando Rastelli[8], Vollrath Martin Axt[3], Juan C. Loredo[4,5], Vikas Remesh[1], Tobias Heindel[2], Doris E. Reiter[6], Gregor Weihs[1]

[1*]Institut für Experimentalphysik, Universität Innsbruck, 6020 Innsbruck, Austria.

[2]Institute of Solid State Physics, Technische Universität Berlin, 10623 Berlin, Germany.

[3]Theoretische Physik III, Universität Bayreuth, 95440 Bayreuth, Germany.

[4]University of Vienna, Faculty of Physics, Vienna Center for Quantum Science and Technology (VCQ), Vienna, Austria.

[5]Christian Doppler Laboratory for Photonic Quantum Computer, Faculty of Physics, University of Vienna, Vienna, Austria.

[6]Condensed Matter Theory, Department of Physics, TU Dortmund, 44221 Dortmund, Germany.

[7]Institut für Festkörpertheorie, Universität Münster, 48149 Münster, Germany. [8]Institute of Semiconductor and Solid State Physics, Johannes Kepler University Linz, 4040 Linz, Austria.

*Corresponding author. E-mail: yusuf.karli@uibk.ac.at;
†These authors contributed equally to this work.

Supplementary Methods

Quantum Dot Sample

The sample used contains GaAs/AlGaAs quantum dots (QDs) obtained by the Al-droplet etching method [1] and was grown by molecular beam epitaxy. The QD are embedded in the center of a λ-cavity placed between a bottom(top) distributed Bragg reflector consisting of 9(2) pairs of $\lambda/4$-thick $Al_{0.95}Ga_{0.05}As/Al_{0.20}Ga_{0.80}As$layers with respective thickness of 69/60 nm. The QDs are placed between to $\lambda/2$-thick $Al_{0.33}Ga_{0.67}As$ layers. The QD growth process starts by depositing 0.5 equivalent monolayers of Al in the absence of arsenic flux, which results in the self-assembled formation of droplets. During exposure to a reduced As flux, such droplets locally etch the underlying $Al_{0.33}Ga_{0.67}As$ layer, resulting in ≈ 9 nm-deep and ≈ 60 nm wide nanoholes on the surface. Then the nanoholes are filled with GaAs by depositing ≈ 1.1 nm of GaAs on the surface, followed by an annealing step of 45 s. The temperature used for the etching of the nanoholes was 600 °C. The droplet self-assembly process results in QDs with random position and a surface density of about $2 \times 10^7 \mathrm{cm}^{-2}$, suitable for single QD spectroscopy.

stiX characterization and optimization

To confirm that the collected photons indeed originate from stiX, several characterisation experiments are done, as presented in the following.

Initially, we vary the TPE power, observing Rabi rotations to determine the TPE π power. While maintaining the TPE pulses at this power, we introduce the stim. pulse tuned to the XX energy and scan their relative time delay (see Methods in the main manuscript) from negative (i.e., stim. pulse arrives before the TPE pulse) to positive while recording the generated X photons. Optimum stiX is achieved when the stim. pulse arrives just after the TPE pulse has maximized the XX state occupation. Arriving earlier will not stimulate the de-excitation and a stim. pulse that arrives too late will allow the XX to already decay spontaneously. This explains the observed dependence of the X emission on the temporal delay between TPE and stim. pulses, a sharp increase for short delays and an exponential reduction of the stimulation effect that follows the XX lifetime. In Ref. [2] the optimum delay is about $0.03 \times \tau_{XX} \approx 5$ ps which matches our observations (Supplementary Figure 1**d**). The red (stim. pulse has H polarization), green (stim pulse has V polarization) and blue (no stim. pulse) dots represent the different polarization cases respectively. At time delay ≈ 7 ps we observe nearly two times the photon counts compared to the reX case for an H-polarized stim. pulse, confirming the successful stimulation. Note that, when we stimulate the V-polarization cascade, we are effectively suppressing the collected decay pathway, which shows as a drop in photon counts (see Supplementary Figure 1**d**, green dots).

As the stim. pulse removes the timing jitter from the exciton emission caused by the biexciton decay, one can also observe the effect in the X photon arrival time distribution (Supplementary Figure 1**f**). The standard reX exciton emission (blue line) exhibits an exponential rise time that corresponds to the XX decay time characteristic of the cascaded emission, before decaying exponentially. When adding the stim. pulse (red line) the timing jitter due to the random biexciton decay is removed and the rise time of the exciton vanishes. The exciton now decays right after the arrival of the stim. pulse.

Once the time delay of the stim. pulse is optimized, one can turn to the polarization control. To achieve maximum enhancement, the polarization of the stimulation pulse that controls the emitted X polarization must match the polarization that is collected, while the orthogonal polarization leads to suppression. This is confirmed by rotating the stim. pulse polarization at optimum delay and power by the means of an HWP (figure 1**b**). In reX, the polarization of the excitation pulse does not have an effect on the X emission polarization, as any linear polarization would generate the H and V cascades to the ground state. However, with the stim. pulse polarization, one can direct the emission cascade to arbitrary ratios of X_H or X_V. We observe an oscillatory trend with respect to the HWP orientation, signifying that

the X_H intensity can be controlled via stiX polarization. Note that, while the enhancement increases the emission by a factor of 2, the suppression does not reduce the counts completely. This is also observed in other works on stiX [3] and can be attributed to an imperfect preparation fidelity of the reX, non-ideal stim. pulse polarization control as well as anisotropies in the quantum dot that cause the polarization axes to not be fully orthogonal, such that the stim. pulse also couples with the other polarization axis [4, 5].

Next, we investigate the power dependence of the stim. pulse by setting the TPE pulse to π-power and sweeping the stim. pulse power (figure 1**e**). This is again done for the stim. pulse with horizontal (enhancement, red dots) and vertical (suppression, green dots) polarization. The coherent excitation and de-excitation of the quantum dot states is evidenced by the presence of Rabi rotations as a function of stim. pulse power consistent with previous works [2, 3, 6]. While adding the stim. pulse depopulates the biexciton to enhance or suppress the exciton emission in one polarization, higher TPE powers can re-populate the biexciton state which compensates the effect of the stim. pulse. Thus, the emission also oscillates as a function of stim. pulse pump area.

Finally, we can quantify the photon enhancement at this optimal stiX condition. At first, we switch off the stim. pulse, and record the X photon counts upon TPE pulse power sweep, to observe the reX Rabi oscillations (Supplementary Figure 1**c**, blue dots). At π-power we observe ≈2600 counts. We now introduce the stim. pulse, with its polarization set to H, and perform the TPE power sweep. The red dots in Supplementary Figure 1c represent the recorded photon counts which, at π-power reach ≈5200 counts, clearly demonstrating the expected two-fold enhancement under optimal stiX conditions. Furthermore, we observe that once we switch to orthogonal polarization of the stim. pulse, the recorded photon counts are minimal, which represent the residual photon emission via the V-cascade (Supplementary Figure 1**c**, green dots).

Finally, the hallmark and main motivation of the stiX scheme is the improved indistinguishability that was already shown in the main text. In summary, all these observations consistently confirm the successful realization of the stiX scheme with two pulses spectrally cut from the same ps-laser.

Photon quality

In Supplementary Table 1 we summarize the single-photon purities and indistinguishabilities measured under various excitation conditions of reX and stiX methods. To compute the $g^{(2)}(0)$, we first fit the recorded photon coincidences for a time interval of $8\,\mathrm{ns}$ around zero delay with a Gaussian function, and also the four side peaks (corresponding to time delays $\pm 12.5\,\mathrm{ns}$ and $\pm 25\,\mathrm{ns}$) to then calculate the ratio of the extracted areas. For calculating raw HOM visibility ($\mathrm{V}_{\mathrm{HOM}}^{\mathrm{Raw}}$) , we again fit the recorded photon coincidences for a time interval of $6\,\mathrm{ns}$ at zero delay for parallel and orthogonal configurations and compute the ratio of the extracted areas. Following, the corrected HOM visibility ($\mathrm{V}_{\mathrm{HOM}}^{\mathrm{Corr}}$) for a non-zero $g^{(2)}(0)$ is calculated by the following formula (see [7] for details):

$$V_{HOM}^{Corr} = \frac{V_{HOM}^{\mathrm{Raw}} + g^{(2)}(0)}{1 - g^{(2)}(0)} \tag{1}$$

Quantum Efficiency

The blinking behavior of the quantum dot varies depending on the type of excitation. In Supplementary Figure 2**(a)-(c)** we present the behaviour under resonant excitation, reX and stiX of the exciton state, on the same quantum dot, as measured under a long timescale $g^{(2)}(0)$, denoted here as $g_{\mathrm{LT}}^{(2)}(0)$ [8, 9]. We fit a symmetric exponential function $g^{(2)}(\tau) = \mathrm{A} * \exp\left(-|\tau/\tau_{\mathrm{blinking}}|\right) + \mathrm{B}$ (black solid lines) to extract a blinking timescale τ_{blinking} and $g_{\mathrm{LT}}^{(2)}(0) = \mathrm{A} + \mathrm{B}$. The extracted parameters are listed in Supplementary Table 2.

$$\mathrm{QE} = \frac{t_{\mathrm{on}}}{t_{\mathrm{off}} + t_{\mathrm{on}}} = \frac{1}{g^{(2)}_{\mathrm{LT}}(0)} \tag{2}$$

We calculate that under resonant s-shell excitation, the quantum efficiency of the quantum dots is ≈ 0.35. By introducing reX and stiX, we are able to achieve higher quantum efficiencies of ≈ 0.45 and ≈ 0.46, respectively.

Time control of PNC

Here, we investigate the control of PNC further using the stiX scheme parameters. Initially, we scan the time delay of the stim. pulse and record the X_{H} counts for various TPE pulse powers. The resulting two-dimensional map of the recorded photon counts of X_H photons as a function of TPE power and stim. pulse time delay is displayed in Figure 4b. We observe that the photon counts reach the expected two-fold enhancement (compared to reX case, c.f. Figure 1**c**) at a time delay $\approx 7\,\mathrm{ps}$ when TPE pulse power reaches $\approx 1\pi$. Subsequently, we perform the PNC experiment (see Methods) at every time delay and TPE power, and extract the visibilities (same as in Figure 4c,g in the main manuscript). We then compute the PNC (note that V_{HOM} is assumed constant for all time delays) using the same procedure as explained in Section 4 and 4. The resulting two-dimensional map of the computed PNC values for various time delays and TPE powers is displayed in Supplementary Figure 4d.

To support our observations, we perform additional simulations on the mean expected photons per excitation cycle (X_H) and the PNC. For computational simplicity, omit the two photon modes and the coupling to them, such that the Hamiltonian (4) reduces to $\hat{H} = \hat{H}^{\mathrm{QD}} + \hat{H}^{\mathrm{TPE}} + \hat{H}^{\mathrm{stim}} + \hat{H}^{\mathrm{phonon}}$. This is motivated by the agreement between the PNC and the quantum dot coherence (see Supplementary Figure 2b and Supplementary Figure 3e) by time-integrating the respective elements and normalizing by the decay rate γ_X, i.e.:

$$\begin{aligned} X_H &\approx \gamma_X \int |\rho_{X_H, X_H}| dt \\ \mathrm{PNC} &\approx \frac{\gamma_X}{2} \int |\rho_{g, X_H}| dt. \end{aligned} \tag{3}$$

The results are displayed in Supplementary Figure 4a and 4c, and show an excellent match with our experimental data.

Estimation of λ for PNC extraction from visibility

We compute PNC based on Equation (20), which depends on λ, a quantity that signifies the purity of the state. Following the method in Ref. 28 we extract this parameter by fitting the measured visibility v (c.f. Figure 4c,g), as

$$v \approx \lambda^2 \rho_{0,0} \sqrt{V_{\mathrm{HOM}}} + v_0. \tag{4}$$

Here V_{HOM} is the measured single-photon indistinguishability, v_0 a residual visibility at π power and $\rho_{0,0}$ is approximated by $\rho_{0,0} \approx 1 - \mathrm{N}$ with N being the normalized photon counts measured while sweeping the TPE pulse power. This approximation is valid since the system does not include decay channels that do not end in the ground state and we treat the photon density matrix in a two-dimensional subspace. Fitting equation (4) we obtain $\lambda_{\mathrm{stiX}} = 0.73(3)$ for stiX (displayed as red circles and squares, respectively indicating the measured visibilities from two detectors) and $\lambda_{\mathrm{reX}} = 0.28(2)$ for reX. The results are displayed in Supplementary Figure 3.

Supplementary Tables

Supplementary Table 1 Single-photon purity, measured as $g^{(2)}(0)$, and indistinguishability (HOM Visibility $\mathrm{V}_{\mathrm{HOM}}^{\mathrm{Raw}}$ and $\mathrm{V}_{\mathrm{HOM}}^{\mathrm{Corr}}$) under reX, stiX and s-shell excitation. Uncertainties are extracted from the fitting procedure.

Protocol	TPE power	stim. power	$g^{(2)}(0)$	$\mathrm{V}_{\mathrm{HOM}}^{\mathrm{Raw}}$	$\mathrm{V}_{\mathrm{HOM}}^{\mathrm{Corr}}$
reX	π	-	0.0004(1)	0.58(3)	0.58(3)
stiX	π	π	0.0009(1)	0.95(6)	0.95(6)
stiX	2π	π	0.0003(1)	-	-
s-shell	-	-	0.04(1)	0.88(3)	0.95(5)

Supplementary Table 2 Blinking behaviour analysis for different excitation techniques. Uncertainties are extracted from the fitting procedure.

Protocol	τ_{blinking} / ms	$g_{\mathrm{LT}}^{(2)}(0)$	QE
s-shell	1.601(6)	2.865(5)	0.349(1)
reX	0.0350(3)	2.247(7)	0.445(1)
stiX	0.0326(3)	2.184(7)	0.458(1)

Supplementary Figures

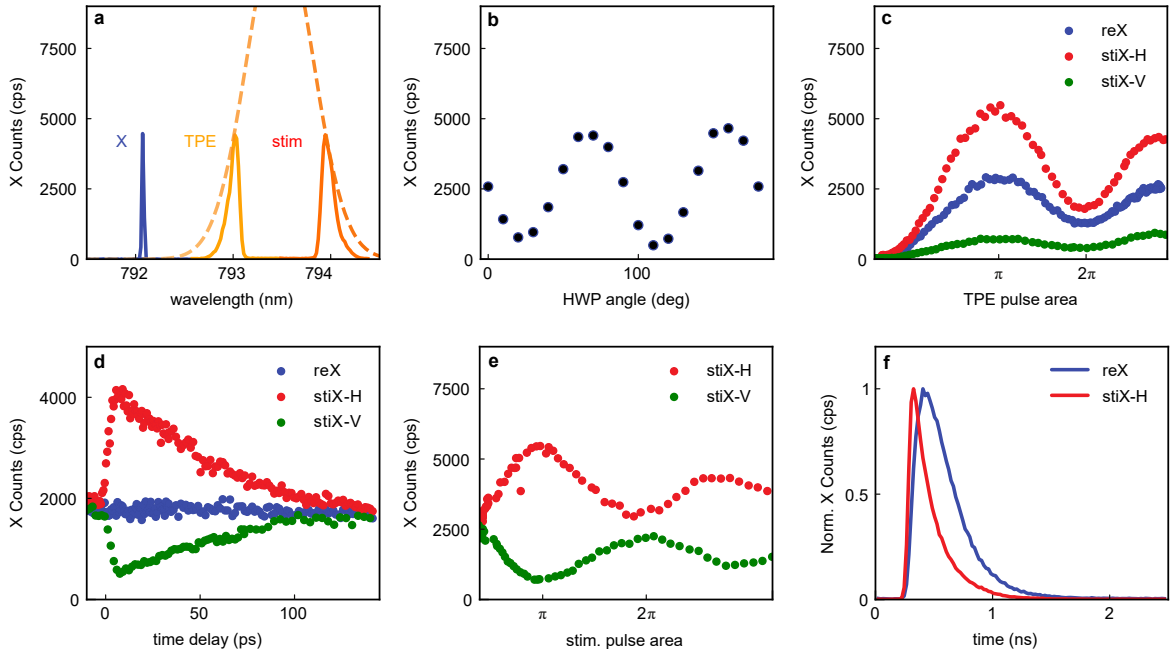

Supplementary Figure 1 stiX characterization: (a) Pulse shaping and detuning during the experiment. TPE (light orange) and stim. (dark orange) pulses are spectrally cut from an initial picosecond pulse (dashed orange line). (b) Integrated X_H counts as a function of the stimulation pulse polarization tuned via an HWP (at optimal delay). (c) Measured two-fold X_H photon enhancement (red dots) under optimal stiX conditions of time delay, power and polarization. The green dots represent the case where we suppress the collected polarisation. Blue dots represent the reX case. (d) Integrated X_H photon counts as a function of the time separation of stim. pulse, following the TPE pulse (red dots). Blue dots represent the X_H photon counts under reX. Green dots represent the drop in photon counts for a vertically polarized stim. pulse. (e) Integrated X_H counts for varying stim. pulse power while keeping the TPE pulse at π power. Red dots represent the H cascade, which is enhanced, while green dots represent the V-polarized cascade, which is suppressed. (f) Emission decay dynamics under stiX (red) compared to reX (blue) in a lifetime measurement.

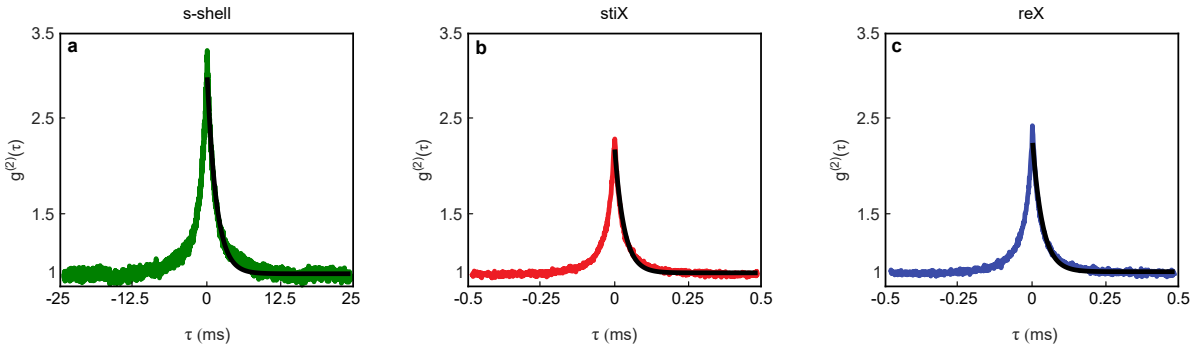

Supplementary Figure 2 Quantum efficiency: Blinking behaviour of the quantum dot under different excitation schemes, as measured by long timescale $g^{(2)}(\tau)$. (a): resonant s-shell excitation, (b): stiX, and (c): reX . Black curve denote the fit.

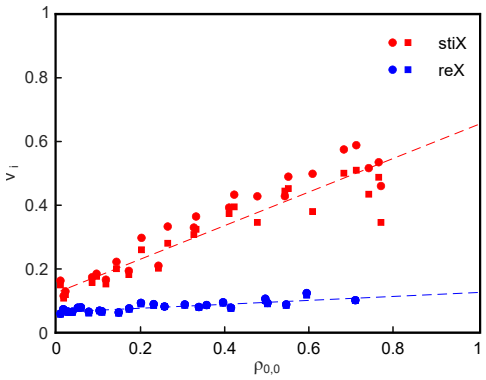

Supplementary Figure 3 Computing λ: Squares (circles) represent the measured visibilities $v_{1(2)}$ measured at APD1(2) respectively. Red and blue denote stiX and reX processes. Dashed lines are linear fits according to equation 4.

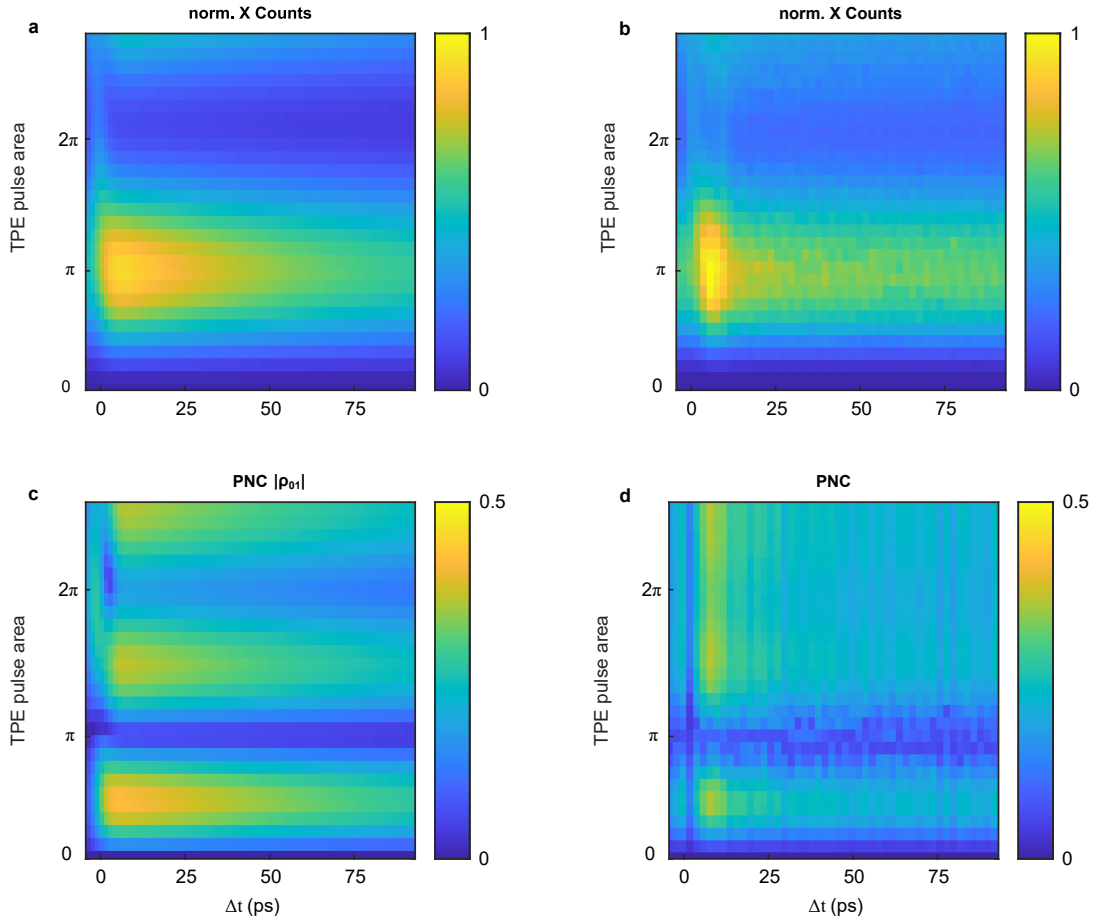

Supplementary Figure 4 stiX and PNC temporal behaviour: (a) **Theory**: Mean photon number per excitation cycle as a function of TPE pulse power and time delay between TPE and stim pulses (Δt). Every column represents the photon number obtained from a TPE pulse power sweep and each row for the corresponding stiX time delay scan, when the stim pulse is at π power (see Supplementary Methods - Time control of PNC for details on calculations.) (b)**Experiment**: Measured X photon counts for the same parameters as in (a). (c) **Theory**: The simulated PNC generated via stiX excitation as a function of stim pulse time delays and TPE pulse areas (see Supplementary Methods - Time control of PNC for details on calculations). (d) **Experiment**: Qualitative extraction of PNC from the extracted visibilities (see main manuscript Fig. 4 and Supplementary Methods- Time control of PNC.) For simplicity, V_{HOM} is considered a constant for all the Δt values.

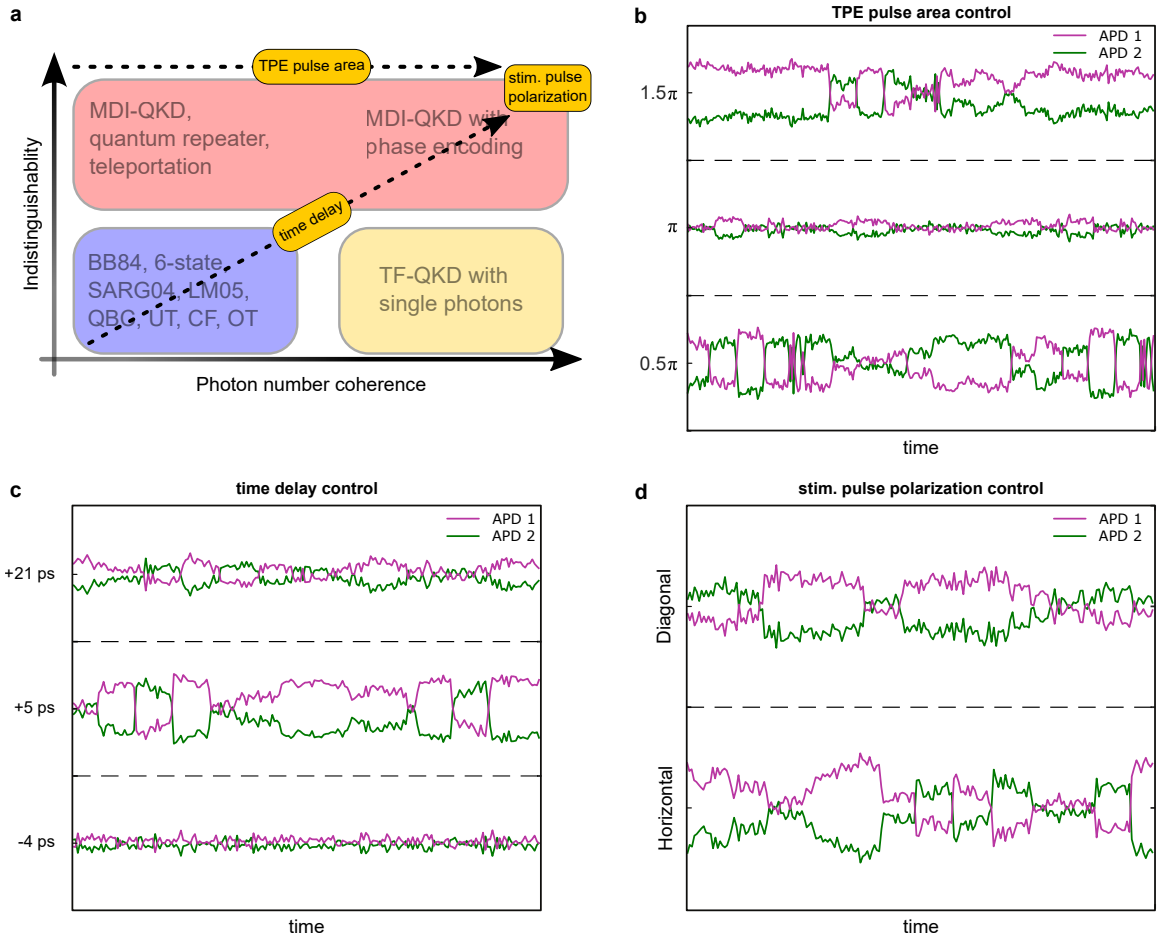

Supplementary Figure 5 Extended Data 2, **versatility of stiX control knobs in exploring the quantum cryptography universe**: (a) With *TPE pulse area*, one maintains high indistinguishability while tailoring the degree of PNC from minimum to maximum (as evidenced in (b) with three exemplary time traces measured on APD1 and APD2, respectively denoted by purple and green curves. See also main manuscript Fig. 4 for more details). The *time delay* of the stim. pulse with respect to the TPE pulse facilitates the control of both the indistinguishability and PNC of the emitted photons ((c) shows three representative time traces measured for stim. pulse time delays -4 ps, 5 ps, and 21 ps. See also Fig.4 for more details). The *polarization control* permits both high PNC and high indistinguishability in the chosen polarization basis ((d) shows the measured time traces for diagonal (D) and horizontal (H) polarization respectively).

Supplementary References

[1] Saimon Filipe Covre da Silva, Gabriel Undeutsch, Barbara Lehner, Santanu Manna, Tobias M Krieger, Marcus Reindl, Christian Schimpf, Rinaldo Trotta, and Armando Rastelli. Gaas quantum dots grown by droplet etching epitaxy as quantum light sources. *Appl. Phys. Lett.*, 119(12):120502, 2021.

[2] Friedrich Sbresny, Lukas Hanschke, Eva Schöll, William Rauhaus, Bianca Scaparra, Katarina Boos, Eduardo Zubizarreta Casalengua, Hubert Riedl, Elena Del Valle, Jonathan J Finley, et al. Stimulated generation of indistinguishable single photons from a quantum ladder system. *Phys. Rev. Lett.*, 128(9):093603, 2022.

[3] Yuming Wei, Shunfa Liu, Xueshi Li, Ying Yu, Xiangbin Su, Shulun Li, Xiangjun Shang, Hanqing Liu, Huiming Hao, Haiqiao Ni, Siyuan Yu, Zhichuan Niu, Jake Iles-Smith, Jin Liu, and Xuehua Wang. Tailoring solid-state single-photon sources with stimulated emissions. *Nat. Nanotechnol.*, 17(5):470–476, 2022.

[4] DN Krizhanovskii, A Ebbens, AI Tartakovskii, F Pulizzi, T Wright, MS Skolnick, and M Hopkinson. Individual neutral and charged in x ga 1- x as- ga as quantum dots with strong in-plane optical anisotropy. *Phys. Rev. B*, 72(16):161312, 2005.

[5] Thomas Belhadj, Thierry Amand, Alejandro Kunold, C-M Simon, T Kuroda, Marco Abbarchi, T Mano, K Sakoda, Sergej Kunz, Xavier Marie, et al. Impact of heavy hole-light hole coupling on optical selection rules in gaas quantum dots. *Appl. Phys. Lett.*, 97(5):051111, 2010.

[6] Junyong Yan, Shunfa Liu, Xing Lin, Yongzheng Ye, Jiawang Yu, Lingfang Wang, Ying Yu, Yanhui Zhao, Yun Meng, Xiaolong Hu, et al. Double-pulse generation of indistinguishable single photons with optically controlled polarization. *Nano Lett.*, 22(4):1483–1490, 2022.

[7] H. Ollivier, S. E. Thomas, S. C. Wein, I. Maillette de Buy Wenniger, N. Coste, J. C. Loredo, N. Somaschi, A. Harouri, A. Lemaitre, I. Sagnes, L. Lanco, C. Simon, C. Anton, O. Krebs, and P. Senellart. Hong-ou-mandel interference with imperfect single photon sources. *Phys. Rev. Lett.*, 126:063602, Feb 2021.

[8] Julian Münzberg, Franz Draxl, Saimon Filipe Covre da Silva, Yusuf Karli, Santanu Manna, Armando Rastelli, Gregor Weihs, and Robert Keil. Fast and efficient demultiplexing of single photons from a quantum dot with resonantly enhanced electro-optic modulators. *APL Photonics*, 7(7):070802, 2022.

[9] Christian Schimpf, Marcus Reindl, Daniel Huber, Barbara Lehner, Saimon F. Covre Da Silva, Santanu Manna, Michal Vyvlecka, Philip Walther, and Armando Rastelli. Quantum cryptography with highly entangled photons from semiconductor quantum dots. *Sci. Adv.*, 7(16):eabe8905, April 2021.